



# Numerical study of hydraulic fracturing on single-hole shale under fluid–solid coupling

Xi Xia · Zhonghu Wu · Huailei Song ·  
Wentao Wang · Hengtao Cui · Motian Tang

Received: 30 May 2022 / Accepted: 10 January 2024  
© The Author(s) 2024

**Abstract** To investigate the hydraulic fracture extension pattern of single-hole shale during hydraulic fracturing under fluid–solid coupling, this paper utilizes seepage–stress–damage coupling software to establish a mechanical model of hydraulic fracture initiation in single-hole shale under different pore pressure increments in seven groups. The results reveal that under the action of a single-hole pressure gradient, shale is destabilized and destroyed by shale instability after two damage degradations under the coupled action of hydraulic and peripheral pressures, the fracture network is fully developed, and the stress decreases sharply. The final damage pattern of the hydraulic fracture distribution is categorized into two types: “X” and “Y”. The hydraulic gradient under hydraulic fracturing is distributed as a closed-loop strip, the hydraulic gradient decreases layer by layer from the inside to the outside, the seepage field and stress field interact with each other, and the pore water pressure and stress are coupled with each other, resulting in increasingly complete fracture development.

## Article highlights

- (1) Single-hole shale under flow–solid coupling for hydraulic fracture testing via RFPA<sup>2D</sup>-Flow software is studied.
- (2) The content and distribution of brittle minerals in shale reservoirs affecting hydraulic fracture extension are studied.
- (3) Damage stress analysis of shale under the coupling of pressure and pore water pressure is completed.

**Keywords** Shale · Fluid–solid coupling · Hydraulic fracturing · Quartz filling · Numerical simulation

## 1 Introduction

Shale gas is a vital nonconventional natural gas resource that is mainly stored in shale formations or mud shale as free or adsorbed gas and can be used in a wide range of applications (Wu et al. 2023), such as residential gas, heating, power generation, automotive fuel and chemical production (Slatt and Rodriguez 2012; Changtao et al. 2017; Pan and Connell 2015). After the drilling of shale gas wells is complete, only a few wells with particularly well developed natural fractures can be directly produced. The underlying reason is the low permeability of the shale matrix (generally less than 1 mu), which makes exploration

---

X. Xia · Z. Wu (✉) · H. Song · W. Wang · H. Cui ·  
M. Tang  
College of Civil Engineering, Guizhou University,  
Guiyang 550025, Guizhou, China  
e-mail: wuzhonghuz@163.com

and development difficult. More than 90% of the wells need to undergo reservoir modification, such as acidizing and fracturing, to obtain more desirable production, and shale reservoirs are usually deeply buried and large and are characterized by a high confining pressure, fine pore throats and extremely low permeability of the shale matrix (Jiu et al. 2013; Yakaboylu et al. 2020). The world has abundant shale gas resources, and shale oil has become a focus for unconventional oil and gas development (Arthur and Asiedu-Okantah 2021; Kazemi et al. 2019; Orozco et al. 2018; Tong et al. 2021; Xie and Zhao 2021; Yu et al. 2021). Among these reserves, China's recoverable shale gas reserves rank first in the world, and shale gas resources are widely distributed in hydrocarbon-bearing regions, such as the Sichuan Basin, Ordos Basin and Junggar Basin; additionally, these reserves have broad exploration prospects and great development potential (Yaoru et al. 2002; Zou et al. 2016). Due to the low proportion of natural gas in primary energy, China has been using coal as its main energy source. Currently, China must vigorously develop natural gas to ensure the security of the energy supply and develop a low-carbon economy (Chai et al. 2019; Li et al. 2021; Liu et al. 2019).

The physical characteristics of the low porosity and low permeability of shale gas reservoirs restrict the flow of internal gas, and the use of hydraulic fracturing technology to form a fracture network inside shale reservoirs is the key to achieving successful shale gas development. Due to the complex geological and tectonic conditions of organic-rich shale reservoirs in China, the physical properties of shale vary greatly among different blocks, and their mechanical parameters exhibit obvious anisotropic characteristics; therefore, the conventional mechanism for hydraulic fracturing fracture expansion in shale reservoirs cannot be fully applied. Thus, it is important to conduct experimental research on the anisotropic properties of shale matrices and fracture expansion mechanisms of hydraulic fracturing and to determine the mechanical properties of shale reservoirs to investigate the fracture initiation conditions, expansion patterns and factors influencing hydraulic fracturing for the successful development of shale gas (Ke-Wei et al. 2015).

Currently, hydraulic fracturing is a promising method for increasing the production of oil and gas wells and has a wide range of applications (Zhao

et al. 2014). Numerical simulation of fracture networks formed by hydraulic fracturing has been challenging because hydraulic fracturing is a complex physical process that includes not only the destruction of the rock mass and fluid–solid coupling but also the interaction of artificial fractures with native natural fractures. In recent years, many scholars at home and abroad have used numerical simulation methods to carry out extensive work on the hydraulic fracturing process and have achieved corresponding results. Olson et al. (2015) studied the intersection of fractures due to hydraulic fracturing and natural fractures in the process of horizontal well fracturing by using a two-dimensional DDM model with correction factors and by considering the uniform hydraulic pressure and fracture height. Weng et al. (2011) used a DDM model to numerically simulate the deformation and propagation of fractures due to hydraulic fracturing and concluded that the intersection of fractures due to hydraulic fracturing and natural fractures is affected by in situ stress and fracturing parameters. For example, Ma et al. (2016) reported that the direction of the minimum principal stress and the difference between the maximum and minimum horizontal stresses both significantly affect the propagation of hydraulic fractures. Zhigang et al. (2012) noted that the viscosity of the fracturing fluid has little effect on fracture propagation, but the injection pressure and elastic film volume of the fracturing fluid have significant effects on the propagation of hydraulic fractures. Jiang (2016) established a three-dimensional numerical simulation of hydraulic fractures to ascertain the influence of different geological and operating factors on the fracture propagation in a coalbed methane reservoir, and the results showed that the greater the difference between the elastic modulus and fracture toughness was, the stronger the inhibitory effect on the extension of the main fractures was; however, this difference was conducive to the formation of more induced fractures. Bu et al. (2019) used RFPA<sup>2D</sup> to study the hydraulic splitting process of heterogeneous rock masses under different perforation angles, which was consistent with the theoretical solution of the optimal perforation angle.

These studies have neglected the mutual coupling between media deformation and the fluid skeleton and the mutual coupling between seepage and stress fields in the actual seepage process of shale in hydraulic fracturing. Therefore, in studying the

pattern of change between the shale stress field and seepage field as well as the mechanical properties of shale during the shale damage process, the fracture expansion pattern and the flow trend of the hydraulic gradient map provide a theoretical basis and data support for the optimal design of hydraulic fracturing in shale gas reservoirs and control of the geometry of the fracture network.

## 2 Regional geological setting

### 2.1 Regional geological characteristics

Fenggang shale gas block three is located in northern Guizhou Province. This area is an important part of the pilot test area project of the National Shale Gas Resources Strategic Survey. It has good geological research foundation and resource development prospects. The main characteristics of the study area are early subsidence, late uplift, a long subsidence period and a short uplift period. The study area shows the long-term development and continuous evolution of the superposition of a marine–continental complex. Due to the repeated superposition of multistage tectonic movements, the Yangtze Platform has complex structural forms. The Qianbei region is geotectonically located in the upper Yangzi platform area. The geology of the two areas has some connectivity.

Therefore, the Yangzi platform also features a complex tectonic pattern in the Qianbei region. The lower Cambrian Niutitang Formation is a widely developed formation in Guizhou Province, and it is the main target layer for shale gas development. The lower Cambrian Niutitang Formation is the most widely distributed black shale series in Guizhou. It is characterized by a large thickness, high organic matter abundance and maturity. The lithologies are mainly gray–black shale, carbonaceous shale, siliceous shale, and silty shale with argillaceous siltstone and siltstone. Figure 1 shows a map of the area of the three blocks in Fenggang, Qianbei, and Guizhou.

### 2.2 X-ray mineral diffraction analysis of the cores

Shale is a sedimentary rock that contains large amounts of organic matter and is composed primarily of clay minerals and quartz minerals (Alafnan 2022). The clay minerals within shale have a large specific surface area and are capable of adsorbing a large amount of shale gas; the brittle minerals in shale are capable of producing a large number of cracks under stress, which can become important seepage channels for shale gas (Ross and Bustin 2009; Zhang et al. 2020). The mineral composition of the Niutitang Formation shale was analyzed via X-ray diffraction (XRD) experiments on 19 pieces of shale. Figure 2 shows that the mineral composition of Niutitang

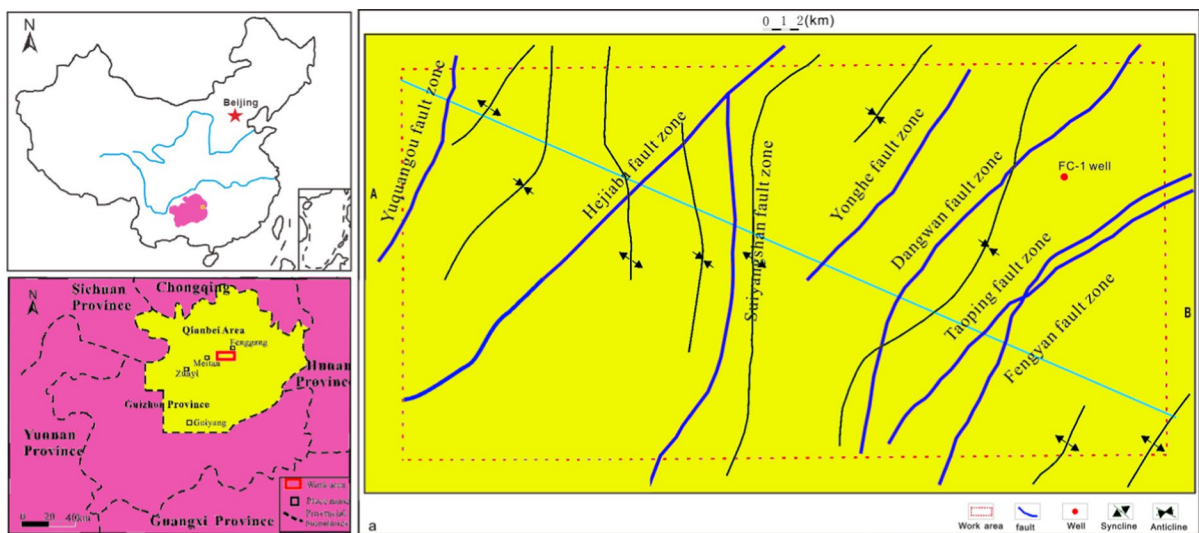


**Fig. 1** Regional map of Fenggang III block in Qianbei, Guizhou Province (Song et al. 2020)

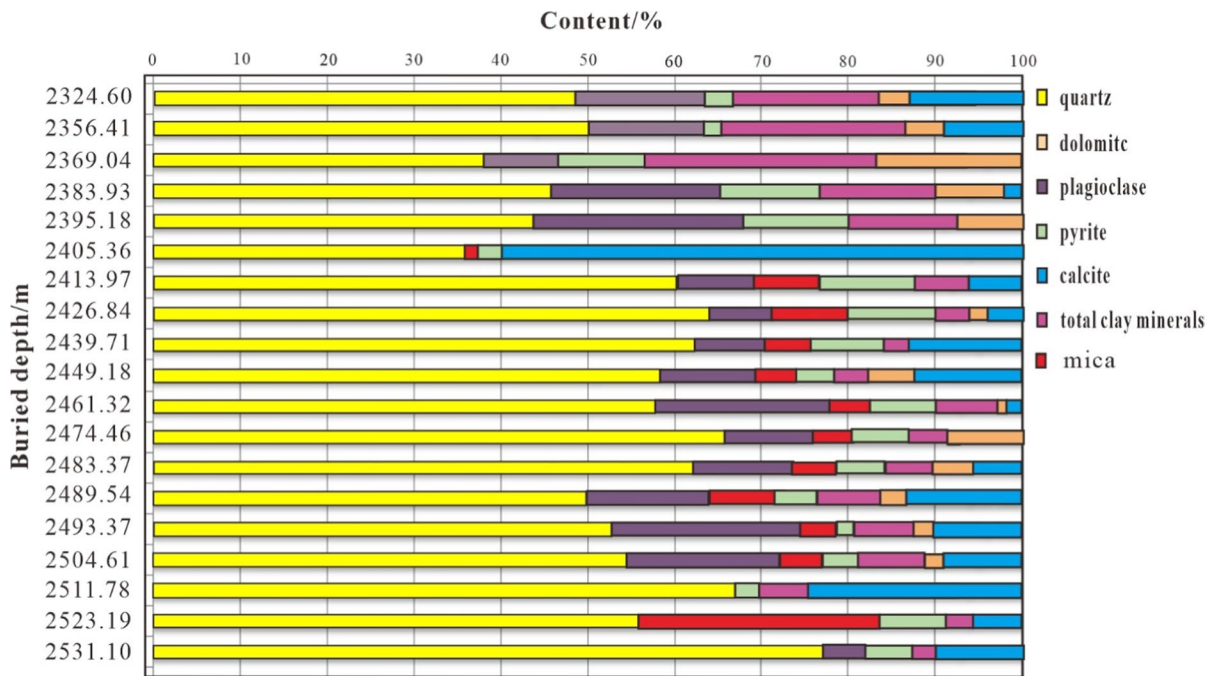


**Fig. 2** Plot of shale mineral composition with depth

Formation shale mainly contains brittle minerals, such as quartz, calcite, feldspar, mica and clay minerals. The quartz contents ranged between 36.21 and 77.32%, with an average content of 58.97%, and the clay mineral contents ranged between 4.76 and 23.76%, with an average content of 10.45%.

### 2.3 Scanning electron microscopy technique

Shale gas occurs in shale pores, which are important storage spaces and circulation channels for shale gas (Wang et al. 2016a) and studying the shale pore structure characteristics and gas-bearing ability is key to understanding the mechanism of shale gas enrichment (Gu et al. 2019; Iqbal et al. 2021). By observing the surface morphology and pore structure of rock samples through scanning electron microscopy, information such as the pore size, morphological characteristics, and distribution can be obtained. The shale samples were scanned by electron microscopy to observe their pore development characteristics. As shown in Fig. 3, the pores in the black shale reservoir of the Niutitang Formation in northern Guizhou Province are dominated by nanoscale pores. The organic matter pores are poorly developed, the pores

are mostly flat and subhedral, the dissolution pores in the organic matter pores are more developed, and strong tectonic activity is conducive to the development of dissolution pores, while fault zones with strong deformation are more likely to produce more dissolution pores and fractures. The pore development characteristics of Niutitang Formation shale are shown in Fig. 3.

## 3 Numerical model

### 3.1 Brief description of the model

Numerical simulation is currently one of the most common and effective methods used to study and model the deformation and damage behavior of geotechnical materials. The numerical simulation software can realistically simulate the whole process of crack initiation, expansion and damage until fracturing (Duan et al. 2006; Tang et al. 2005). The RFPA<sup>2D</sup>-Flow system is a simulation software package based on seepage mechanics equations and elastic damage theory that can simulate the gradual damage process of rock media under varying pore

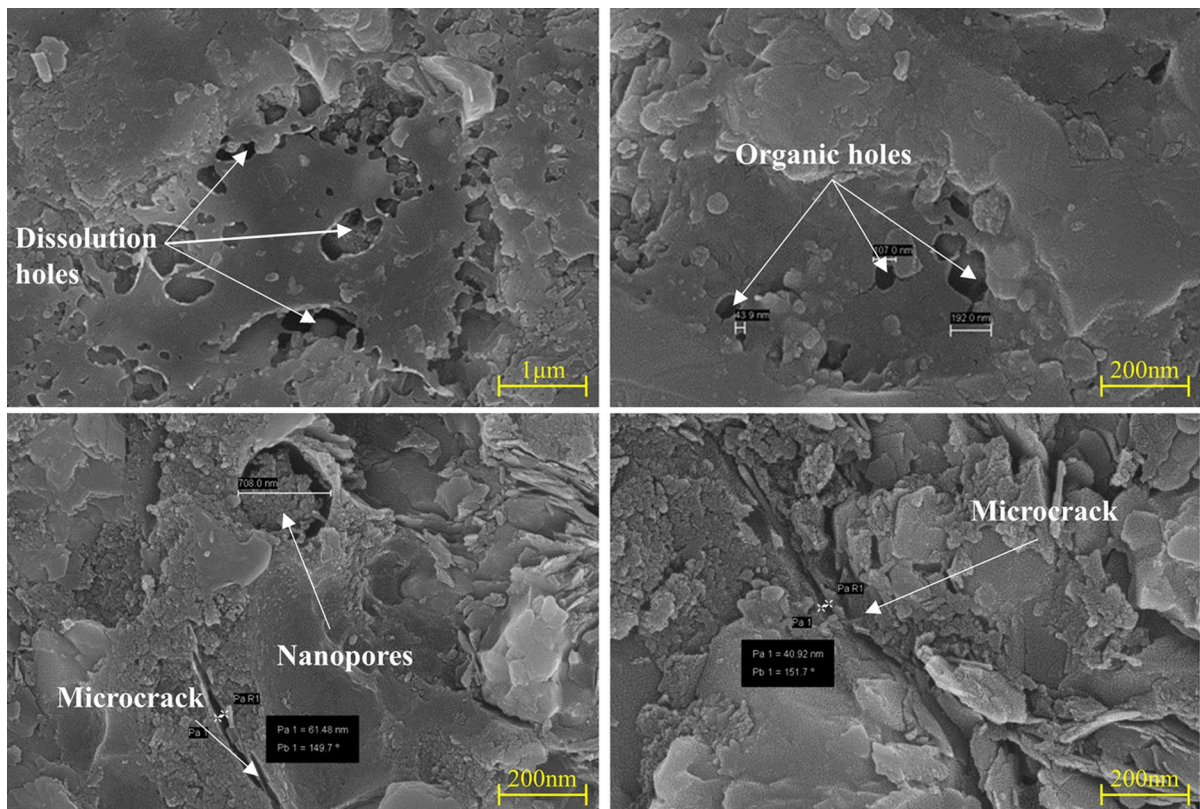


**Fig. 3** Characteristics of shale pore development in Niutitang Formation

water pressures. In addition to the classical Biot coupled equation for seepage mechanics, a modified coupled equation for seepage and strain (rate of change in the pore space) is used in the system calculation. Using the RFPFA<sup>2D</sup>-Flow version of the numerical software, it is assumed that the shale fine-scale unit satisfies the Weibull distribution, the nature of the unit is considered to be linear-elastic-brittle or brittle-plastic, and the other parameters, such as the elastic modulus and strength of the unit, obey certain kinds of distributions, such as the normal, Weber, and uniform distributions.

For the unit permeability-damage coupling equation, when the shear stress reaches the Mohr–Coulomb damage threshold, the damage variable is expressed by the following equation (Xu et al. 2006):

$$D = \begin{cases} 0 & \epsilon < \epsilon_{c0} \\ 1 - \frac{f_{cr}}{E_0 \epsilon} & \epsilon_{c0} \leq \epsilon \end{cases} \quad (1)$$

In the formula,  $f_{cr}$  is the uniaxial compressive residual strength and  $\epsilon_{c0}$  is the maximum compressive strain.

The experiments show that the damage causes the permeability coefficient of the specimen to increase sharply, and the change in the permeability coefficient can be described as follows:

$$\lambda = \begin{cases} \lambda_0 e^{-\beta(\sigma_1 - \alpha\rho)} & D = 0 \\ \zeta \lambda_0 e^{-\beta(\sigma_1 - \alpha\rho)} & D > 0 \end{cases} \quad (2)$$

In the formula,  $\lambda_0$  is the initial permeability coefficient;  $\rho$  is the pore pressure; and  $\zeta$ ,  $\alpha$ , and  $\beta$  are the permeability coefficient rate of increase, pore pressure coefficient and coupling coefficient, respectively.

The problem of groundwater seepage in rock fractures can be modeled by following Darcy’s law for the seepage problem.

$$Q = Kw \frac{h}{L} = KwI \quad (3)$$

In the formula,  $Q$  is the infiltration flow rate,  $w$  is the water cross-section,  $h$  is the head loss,  $L$  is the infiltration path,  $I$  is the hydraulic gradient, and  $K$  is the infiltration coefficient.

### 3.2 Model validation

RFPFA<sup>2D</sup>-Flow numerical simulation software is a suitable tool for studying hydraulic fracturing behavior. Xu et al. (2015) numerically simulated a circular borehole in a nonhydrostatic stress field, and by comparing the numerical simulation results and analyzing the Kirsch solution, it was concluded that the software is suitable for studying hydraulic fracturing. It is suitable not only for the stress fields induced around boreholes but also for the initiation and propagation patterns of hydraulic fracturing. In addition, the coupled flow, stress and damage (FSD) model in the RFPFA simulation has been validated in previous publications (Tang et al. 2002; Noghabai 1999; Wang et al. 2016b; Rabczuk et al. 2010; Thallak et al. 1991; Yu et al. 2016).

Comparing the numerical simulation results with the experimental results (Zhang et al. 2019), the experimental setup has a horizontal stress difference

of 1.5 MPa, and the numerical simulation in this paper sets up a horizontal stress difference of 0 MPa. As shown in Fig. 4, the simulation curve in this paper shows stronger plasticity, and it can be seen that the overall upward and downward trends of the pump pressure curve and the stress curve obtained by numerical simulation are similar, and the peak stress of the final failure is relatively similar, with the simulated value of 73.04 MPa, the experimental value of 63.12 MPa, and the error of 13.58%. In summary, the numerical model can well simulate the hydraulic fracturing characteristics of rocks.

### 3.3 Mechanical modeling

In this study, a numerical model was developed based on geological data from the Niutitang Formation in Fenggang shale gas block 3, Guizhou. As shown in Fig. 5, the model is a two-dimensional numerical model (30 mm in length and 30 mm in height) divided into a grid of 200×200 cells with a well diameter of 15 mm. To study the influence of different loading pore water pressures on the mechanical properties of shale, seven groups with 20% quartz content were established; the confining pressure was

**Fig. 4** Comparison of pump pressure curve between experimental test (Zhang et al. 2019) and numerical simulation

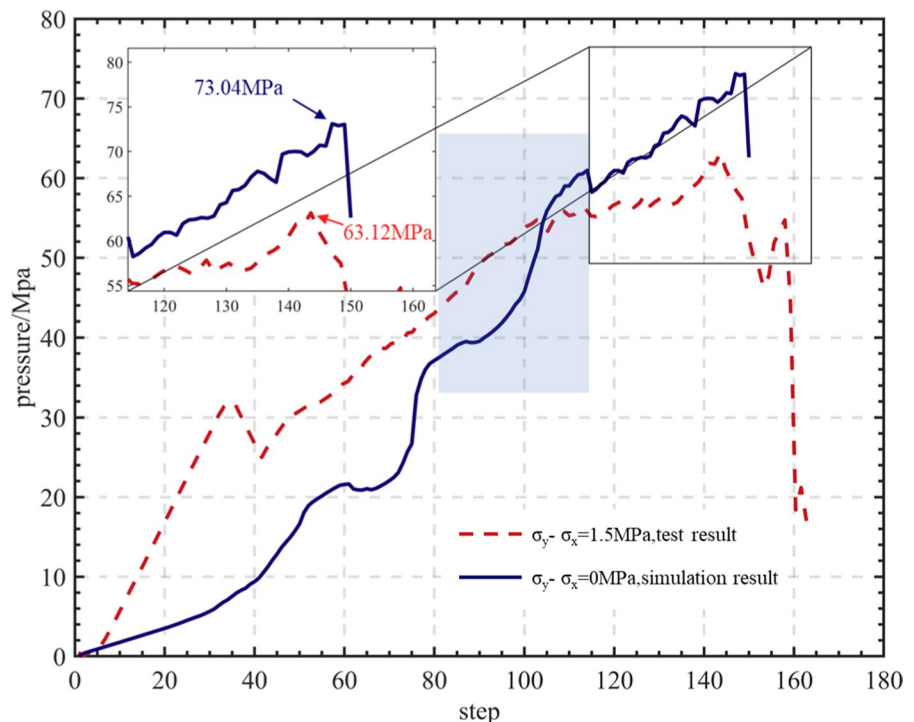
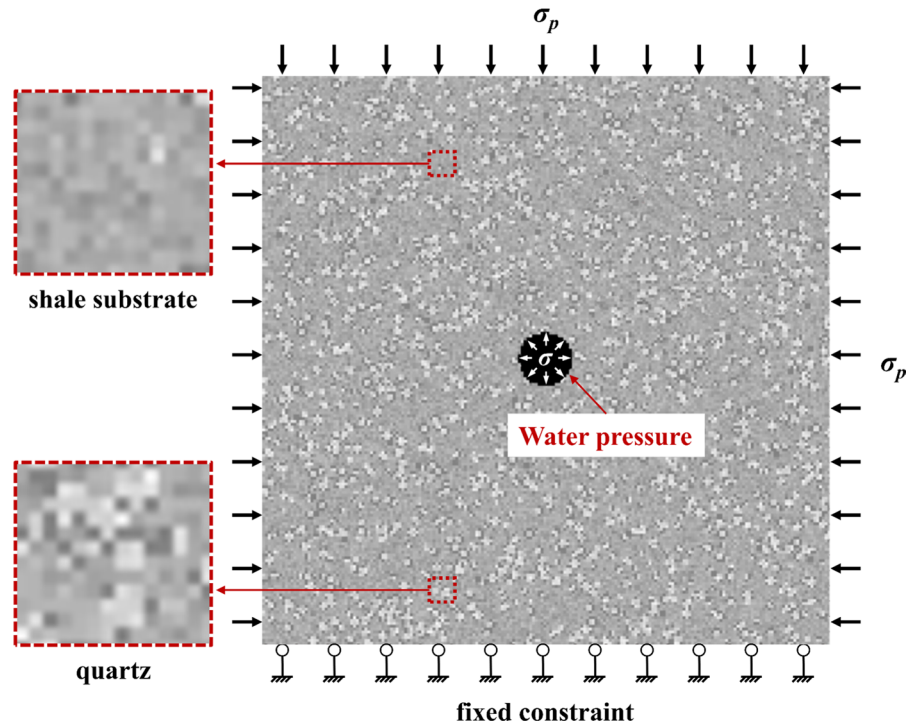


**Fig. 5** Schematic diagram of shale numerical model loading



fixed at 10 MPa; the initial pressure in the hole was 1 MPa; and the loading rates were 0.2 MPa, 0.25 MPa, 0.3 MPa, 0.35 MPa, 0.4 MPa, 0.45 MPa, and 0.5 MPa in each step increment until the shale was completely destabilized and destroyed. In this numerical model, it was assumed that the rock strength and elastic modulus obey the Weibull random distribution (Liu et al. 2021a, 2023a).

$$\varphi(a) = \frac{m}{a_0} \left(\frac{a}{a_0}\right)^{m-1} \exp\left[-\left(\frac{a}{a_0}\right)^m\right] \quad (4)$$

In the formula,  $\varphi(a)$  is the statistical distribution density of the mechanical properties of microscopic

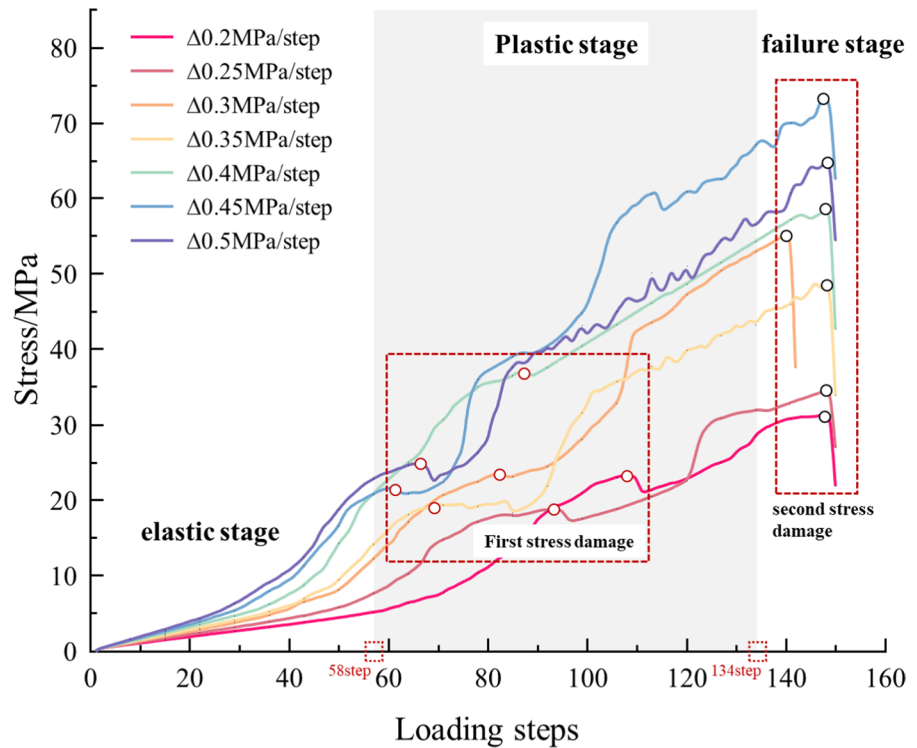
elements  $a$ ,  $a_0$  is the average value of the mechanical properties of the microelements,  $a$  is the mechanical property parameter representing the microunit, and  $m$  is the uniformity coefficient.  $m$  is an important parameter affecting the macroscopic response of numerical samples;  $m$  and  $a_0$  must be determined according to the actual macroscopic strength of shale.

The shale is filled with quartz, resulting in its respective internal nonuniformity. To be fully reflected in the test process, the Monte Carlo method is used to assign values for the finite element mesh element. The initial mechanical parameters of the shale reservoir are shown in Table 1 below.

**Table 1** Material parameters of microscopic media in shale (Wu et al. 2021)

Input parameters	Shale matrix	Quartz particle
Homogeneity index, $m$	5	8
Young's modulus, $E$ (MPa)	51600	96000
Uniaxial compressive strength, $f_c$ (MPa)	147	375
Angle of internal friction, $\psi$ (°)	35	60
Ratio of compressive-tensile strength of rock, C/T	14	15
Poisson's ratio, $\mu$	0.22	0.08

**Fig. 6** Stress-loading step relationship of shale in a single hole under different water pressure increments



## 4 Results and discussion

### 4.1 Evolution pattern of damage to the shale strength

According to the results of the numerical simulation experiments, the loading steps and stress changes in the single-hole shale under the different pore water pressure increments are obtained, as shown in Fig. 6. The graph shows that the stress generally increases as the loading step increases. Like the conventional rock stress curve, the curve undergoes three stages: the elastic phase, the plastic phase, and the failure phase. However, there is an interesting phenomenon in the plastic phase in which a small decrease in the stress curve occurs for the first time between loading steps 60 and 110, followed by an increase in the stress curve, which continues to increase and indicates strong plasticity; this phenomenon is defined by the author as initial stress damage. The phenomenon is that the pore water pressure inside the circular hole exceeds the maximum tensile strength of the shale, the shale appears to be damaged by local tension, and some of the stresses are released in the form of deformation; moreover, the whole pore pressure remains stable under circumferential pressure, but the shale

appears to be in an intensely plastic state because it has already been damaged.

After the initial stress damage occurs in the shale, the curve continues to increase in a fluctuating pattern as the pore water pressure continues to increase. This is because when cracks have formed in the shale, the pore water pressure in the fractures continues to increase, the fractures continue to expand, and the fractures cannot continue to transmit stress; thus, the stress curve fluctuates and rises. After the stress reaches the maximum strength of the controlling rock surrounding the shale, the stress decreases sharply, which corresponds to the overall penetration of fractures in the shale. In this paper, the author defines this phenomenon as secondary stress damage.

The primary stress damage and the secondary stress damage in Fig. 6 are plotted separately, as shown in Fig. 7, and the relationships between them and the pore water pressure increase are studied. Figure 7a shows the relationship between the initial stress damage and the increase in pore water pressure, and the primary stress damage shows a slight upward trend with increasing pore water pressure. When the pore water pressure increase is 0.4 MPa/step, the initial stress damage increases rapidly to 36.54 MPa,



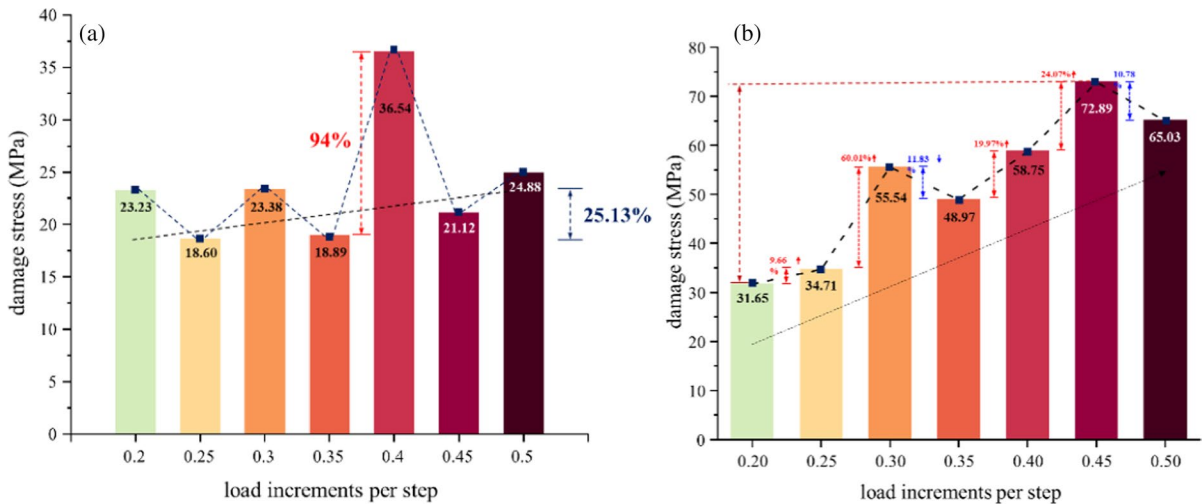


**Fig. 7** Trend of shale damage stress under different water pressure increments; **a** primary stress damage; **b** secondary stress

which is 94% of the initial stress damage corresponding to a pore water pressure increase of 0.35 MPa/step. Figure 7b shows the relationship between the secondary stress damage and hydraulic increase, from which it can be seen that with increasing hydraulic pressure, the secondary stress damage also shows an increasing trend; however, unlike Fig. 7a, the secondary stress damage is more sensitive to the hydraulic pressure increase. When the pore water pressure increases continuously, the water can fill the holes at a slower rate when the pore water pressure increment is small. When a crack occurs, because the circular voids have been filled with water, the water can only be squeezed into the crack, after which the pressure continues to increase, and most of the pressure acts on the inside of the fracture; thus, when the secondary stress damage is low, the shale overall experiences penetration failure. During a continuously increasing pore water pressure, when the pore water pressure increases further, the water has no time to fill all the round voids, and the pressure is already very high. Cracks develop when the pressure is greater than the tensile strength. Because all the pores are not filled with water, only some of the pore water pressure directly acts on the cracks, resulting in overall penetration and destruction of the shale only when the pressure is very high. For the difference between large and small pore water pressure increases, according to the data shown in Fig. 7a, 0.4 MPa/step is the

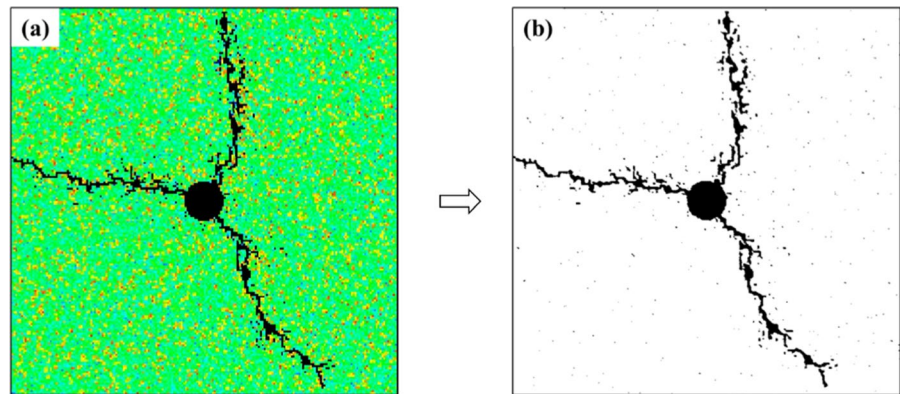
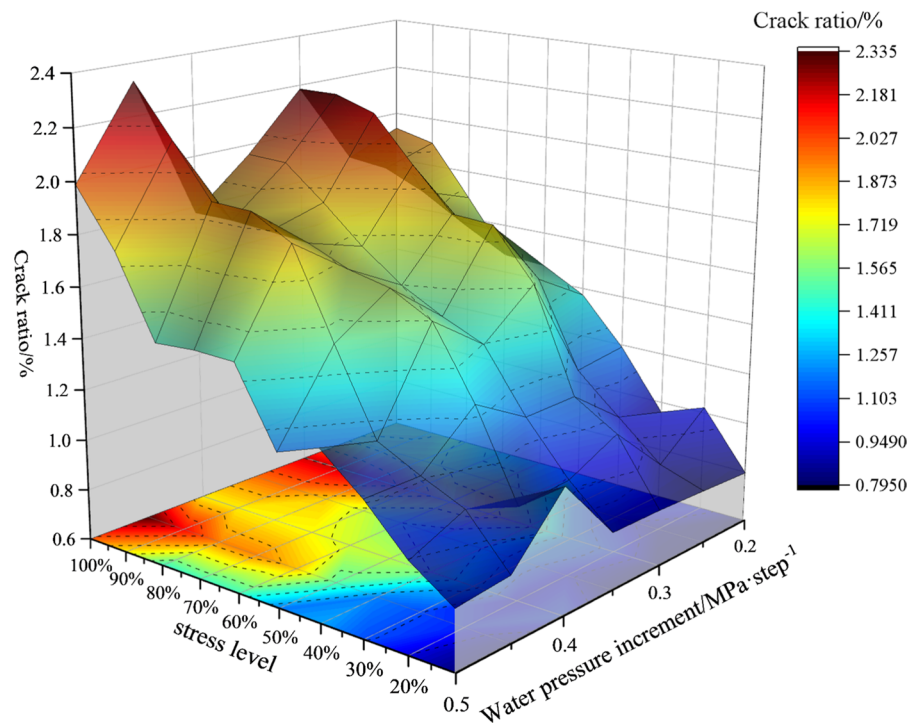
boundary, less than 0.4 MPa/step is a small pore water pressure increase, and greater than or equal to 0.4 MPa/step is a larger pore water pressure increase.

#### 4.2 Quantitative analysis of cracks

The fractal dimension of surface cracks after rock fracturing can be used as a damage characterization factor to measure the degree of material damage and to describe its complexity quantitatively (Liu et al. 2023b; Wang et al. 2022). Larger values indicate more complex crack distributions, more irregular extension paths, or more difficult fragmentation. The effects of hydraulic fracturing can be quantitatively evaluated in terms of fracture rates. Making full use of the extent of fracture expansion is useful for improving the relevance and effectiveness of fracturing design schemes. Improving the fracture extent as much as possible to increase the recovery rate of shale gas during extraction is of great theoretical and practical significance for the hydraulic fracturing and transformation of shale reservoirs.

$$C_r = \frac{S_c - \pi r_a^2}{S_p + \pi r_a^2} \tag{5}$$

where  $C_r$  is the crack rate, in %;  $S_c$  is the black pixel area;  $r_a$  is the radius of the circular hole; and  $S_p$  is the entire model area.

**Fig. 8** Image processing**Fig. 9** Three-dimensional plot of fracture rate-stress level in single-hole shale under different hydraulic pressure increments

Taking the instability destruction at 0.2 MPa in Fig. 10 as an example, the image is processed by ImageJ software, as shown in Fig. 8. The crack morphology is obtained after image processing, and the crack rate is calculated by Eq. (1), with one pixel as 1 unit. To better analyze the rule of change in the crack rate, the calculated results are plotted in Fig. 9. In the figure, a stress level interval of 0–100% on the x-axis represents positive; the start of pressurization is defined as 0%, the maximum stress is defined as 100%, and the middle is divided by an equal distance. The fracture rate tends to

increase with increasing stress. A hydraulic pressure increase of 0.45 MPa/step at a stress level of 100% results in the largest fracture rate of 2.31% and the best hydraulic fracturing effect. The figure shows that the cracking rate curve reaches a maximum at a stress level interval of 70–90% at a hydraulic pressure increase of less than 0.4 MPa/step, but the cracking rate appears to decrease with increasing stress. This phenomenon can be explained well by the stress damage in Sect. 4.1. Although the shale shows the penetration of damage at a lower stress value when the pore water pressure increases are

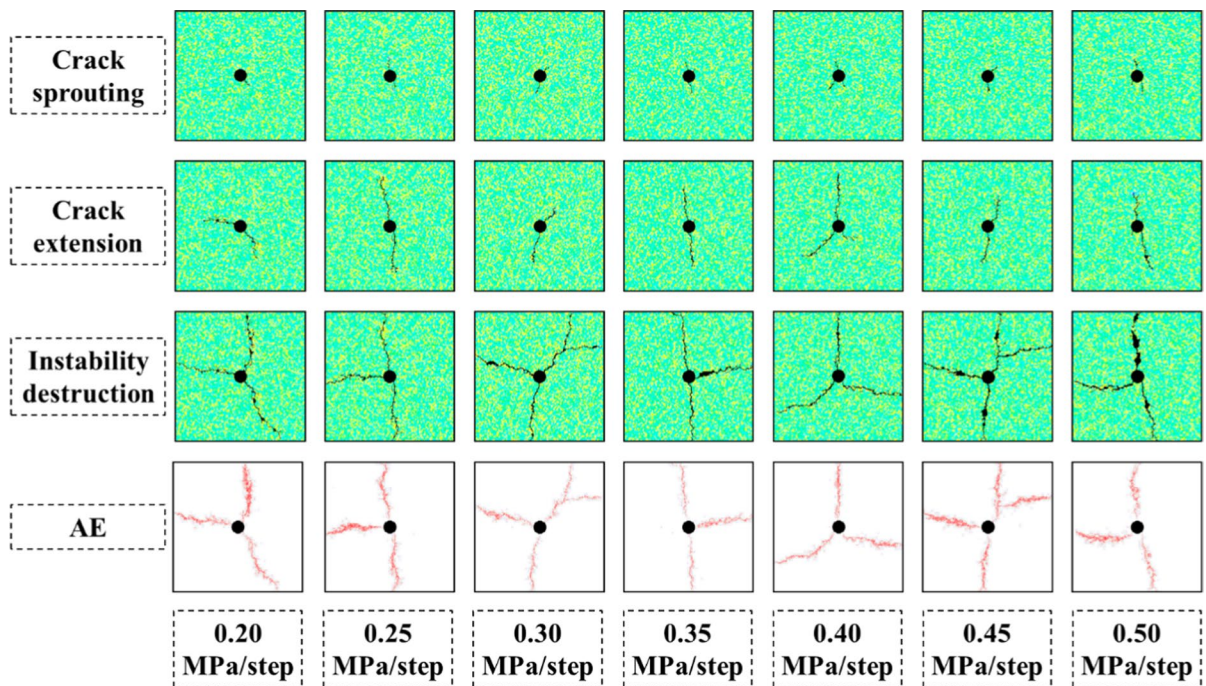


**Fig. 10** Evolution of elastic modulus and acoustic emission diagram of single pore shale under different pore water pressure increments

low, a lack of pressure leads to further densification of the cracks under circumferential pressure. However, this phenomenon does not occur after the pore water pressure increase exceeds 0.4 MPa/step, indicating that a pore water pressure increase greater than 0.4 MPa/step has a certain crack-supporting effect and can maintain an open crack. In addition, the cracking rate is already greater than 1% at a stress level of 10% for a hydraulic pressure increase of 0.4 MPa/step, but a decrease in the cracking rate occurs when the stress level increases to 20%.

#### 4.3 Fracture process of the shale microstructure

After hydraulic fracturing and numerical simulation experiments on shale, according to the characteristics of its destruction process, the whole destruction process is divided into three destruction stages, namely, the fracture emergence, fracture expansion and destabilization destruction stages, which are plotted in Fig. 10. The figure shows that in the crack initiation stage, cracks are generated in the vertical direction, and the initial crack inclination angle determines the direction of the cracks to a certain

extent. Based on the final distribution pattern of the cracks, they are further classified into two categories: X-type and Y-type. The fracture patterns with hydraulic pressure increases of 0.3 MPa/step and 0.45 MPa/step are X-shaped; the fracture patterns with hydraulic pressure increments of 0.2 MPa/step, 0.25 MPa/step, 0.35 MPa/step, 0.4 MPa/step and 0.5 MPa/step are Y-shaped. Due to the random filling of quartz in the shale matrix, the spatial distribution characteristics are significantly random, which causes an uneven distribution of the stress field inside the shale and produces a local stress concentration, leading to the zigzagging expansion path of the cracks. When subjected to external loading, the shale matrix strength is much lower than that of quartz, the shale matrix first sustains damage, or the shale matrix and quartz junction form the weakest part of the initial microcracks; additionally, cracks form along the quartz particles on both sides of the expansion, not directly through the quartz particles, so that the cracks intermittently form zig-zag shapes. Once the cracks sprout, their expansion competes when one of the cracks begins to expand in depth. The crack direction of the pressure area

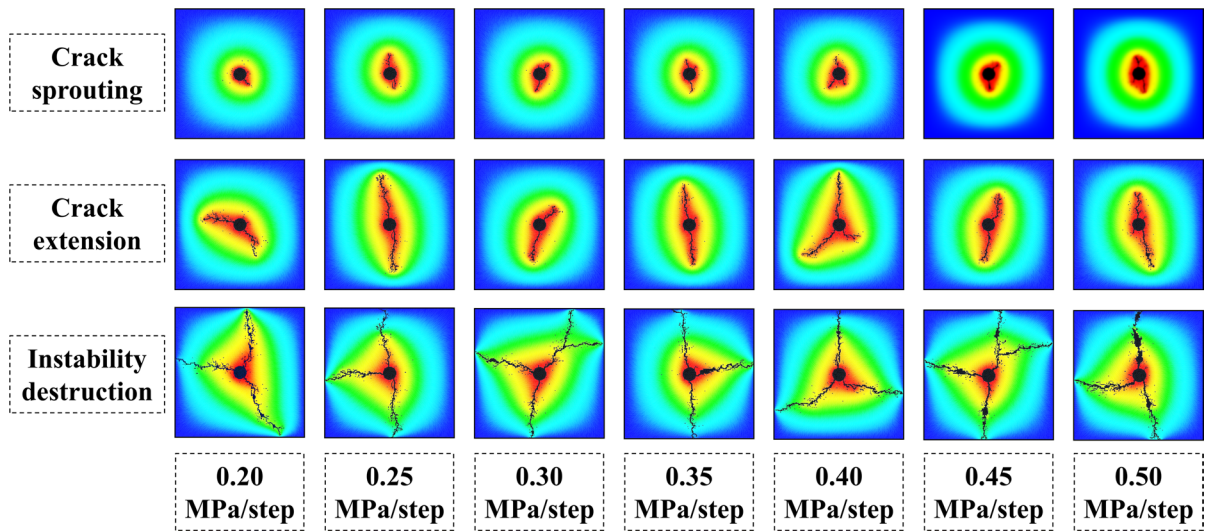


**Fig. 11** Hydraulic gradient of single-hole shale under different pore water pressure increments

increases because of the symmetrical direction of the cracks, which provides the conditions for the expanding cracks around the neighboring cracks to gradually disappear, resulting in the formation of a symmetrical diagonal "Y"-type crack expansion pattern.

Figure 11 shows the hydraulic gradient under the action of pore water pressure. The hydraulic gradient is the head loss per unit infiltration pathway along the direction of water flow. It can be expressed as the ratio of head loss along the infiltration pathway to the length of the infiltration pathway:

$$i = \frac{\Delta h}{\ell} \quad (6)$$

where  $i$  is the hydraulic gradient,  $\Delta h$  is the head loss along the infiltration direction, and  $\ell$  is the infiltration distance.

Since the seepage pressure inside shale is often difficult to measure, the pore water pressure around a borehole is usually used for calculations. According to Darcy's law, the seepage pressure inside the rock mass is considered to decay linearly with permeability distance, and the hydraulic gradient inside the whole test section is a certain value. The figure shows that for the red, green and blue closed loops of the hydraulic gradient, the hydraulic gradient size

decreases from the inside to the outside layer by layer, and the water flows along the preferred path through the microfracture. Once the fractures begin to multiply and continue to expand, fluids first enter the new fractures, facilitating their expansion and splitting as the pore water pressure continues to increase. Since shale contains brittle minerals such as quartz, which randomly fills the shale matrix, the spatial distribution of these minerals is random. The brittle nature of shale allows it to form natural and induced fractures under external forces, with more dense parts of the brittle minerals cracking first. Due to the coupling effect of the stress field and seepage field, in the early stage of loading, the confining pressure is much greater than the pore water pressure, and the stress field dominates. Moreover, the internal initiation of microdamage dominates the shale, changing the seepage field in the specimen. With increasing pore water pressure, the seepage field reacts to the stress field, the shale sustains microdamage, the shale is subjected to complex stresses internally, and damage accumulates. At this time, the internal fracture development in the shale is increasingly accelerated by the creation of new cracks, and macroscopic fractures gradually by contacting each other. Eventually, the fracture network fully develops, and the shale is destabilized and destroyed.

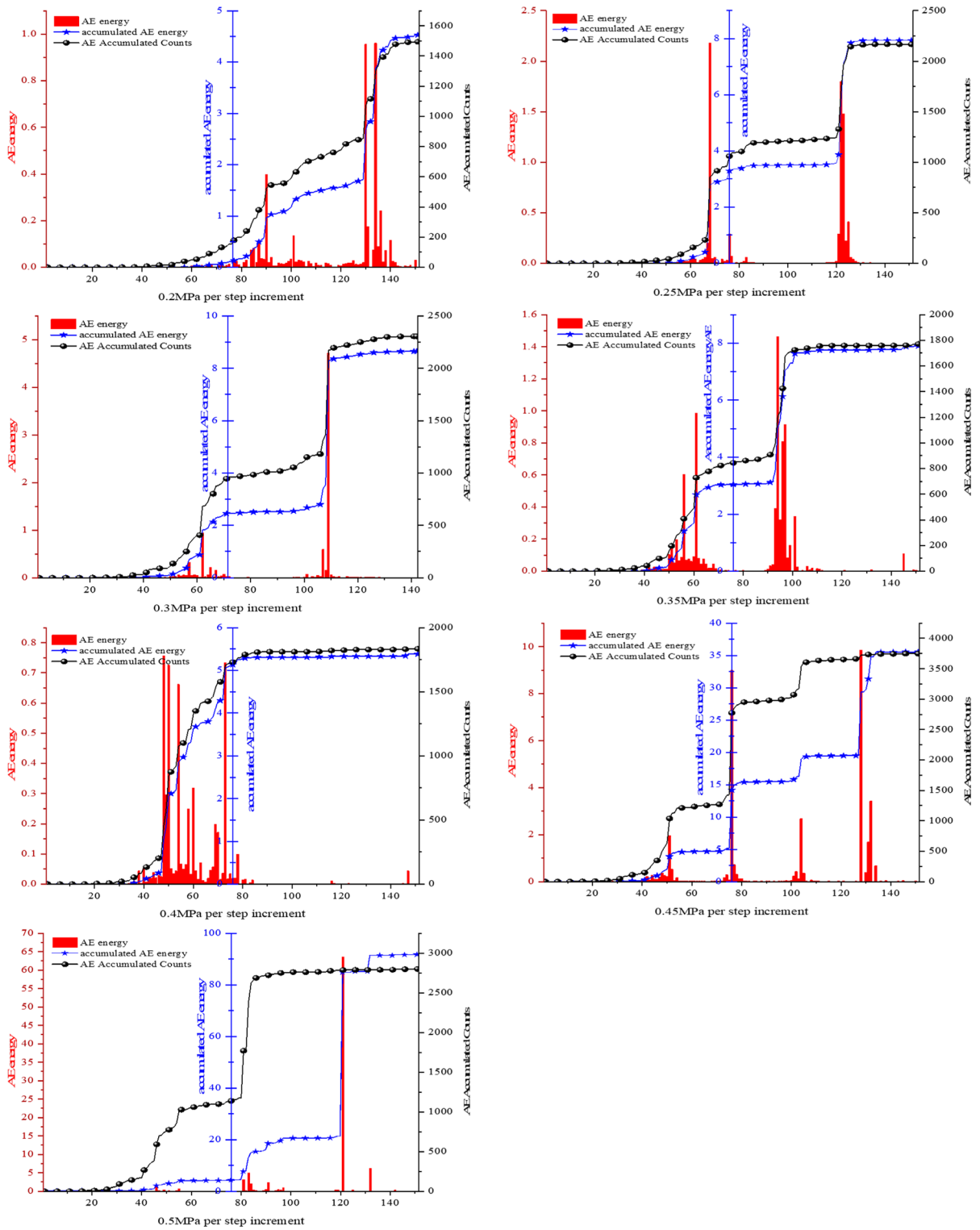


Fig. 12 AE energy, cumulative AE energy, cumulative AE counts versus steps for different single pore shales

#### 4.4 Evolutionary characteristics of the acoustic emission results of shale microstructures

Acoustic emission is a phenomenon in which a localized region in a shale specimen generates a stress concentration that rapidly releases energy and produces transient elastic waves (Liu et al. 2023c). In the model, the microrupture of a cell represents an acoustic emission event (Liu et al. 2021b). The cumulative AE count is the sum of the cumulative acoustic emission events, which indicates the sum of the number of microruptures in each event. Due to its non-homogeneity and the complexity of the constituent structure, the cell presents complex acoustic emission characteristics during the deformation process due to force. As shown in Fig. 12, the cumulative AE counting–loading step is in good agreement with the cumulative AE energy–loading step. During the loading process, the acoustic emissions in each state exhibit obvious differences.

The pore water pressure increases of 0.2 MPa, 0.25 MPa, 0.3 MPa, 0.35 MPa and 0.5 MPa are divided into 5 stages. The cumulative AE energy shows the following pattern: “flat–jump–growth–flat–surge–flat”. In stage 1, the stress level is low, and the AE signal is relatively weak. No acoustic emission or a low number of acoustic emission events and a very low event rate occur. No obvious cracks are produced. In stage 2, the cumulative acoustic emission events exhibit linear growth, and a large number of fresh fine microfractures are formed. In stage 3, the cumulative acoustic emission events exhibit a slight change, and the specimen is not yet damaged. In the fourth stage, the cumulative acoustic emission events surge, the acoustic emission phenomenon is still obvious after the peak intensity, and the number of large events increases rapidly. Continuous expansion of fine microcrack specimens, communication between macroscopic cracks, and rapid destruction of rock bridges between cracks are observed. In stage 5, more acoustic emission events are generated, the AE signal is stronger, and the stress enters the drop stage. The fracture undergoes dramatic extension and expansion until it penetrates, at which point the shale has been completely destroyed.

When the pore water pressure increases by 0.4 MPa per step, the cumulative AE shows a “gentle–surge–stable” pattern. In the first stage, the loading

steps occur in the first 35 steps, no significant acoustic emission signal appears, and the cumulative acoustic emission events show a flat change. In the second stage, the loading steps show a surge in acoustic emission events between 35 and 85 steps, the acoustic emission signal produces a jump with an extremely strong signal, and the stress is in the yielding stage. At this point, microfractures in the shale specimen begin to initiate, indicating that damage occurs in the specimen at this stage. In stage 3, the cumulative acoustic emission event performance stabilizes after 85 loading steps when the shale is completely destroyed.

When the pore water pressure increase is 0.45 MPa per step, the cumulative AE performance follows the “flat–jump–growth–flat–surge–flat–surge–flat” pattern. In phase 1, the initial shale compaction stage, fewer acoustic emission events are produced, and there is a more sporadic distribution within the shale, with cumulative acoustic emission events showing a flat variation. In the second stage, after 40 loading steps, the number of acoustic emission event performance events increases, and the acoustic emission signal is relatively large. When the first damage is reached, the acoustic emission releases an extremely strong signal and generates more events. In stage 3, the acoustic emission event performance tends to stabilize, the acoustic emission phenomenon occurs during a relatively calm period before the peak intensity, and no obvious cracks are produced. In stage 4, when the loading step reaches 75 steps, the acoustic emission events appear to surge, and microscopic fractures form inside the shale. As the pore water pressure increases, the shale continues to extend and expand, and fracture development becomes obvious. In stage 5, the loading steps are in the 75–108 step interval, the acoustic emission events recover smoothly, and the shale is in the late stage of fracture expansion. In the 6th stage, the loading is at 108 steps when the acoustic emission events surge, and the signal released by acoustic emission is extremely strong and generates more events. The microscopic fractures within the shale are strongly connected until they penetrate, and the shale is destabilized and destroyed. In stage 7, after 108 loading steps, the cumulative acoustic emission events exhibit a flat change, and the specimen is completely destroyed.

## 5 Conclusion

In this paper, the RFPA<sup>2D</sup>-Flow real fracture analysis system is used to establish seven sets of numerical simulation experiments under the influence of different pore water pressure increments to study the mechanical properties of monoclinic shale under different pore water pressures and to determine the damage pattern and quantitative analysis of the fracture rate. The following conclusions are drawn:

- (1) In shale, peripheral pressure and pore water pressure are coupled after two damage events, shale reaches the initial damage stress level, energy is released, and stress drops. After reaching the second damage stress level, that is, at the peak stress, the crack network fully develops, the stress decreases sharply, and shale instability occurs.
- (2) The hydraulic gradient of single-hole shale under hydraulic fracturing in different intervals is distributed in closed-loop strips, and the hydraulic gradient decreases layer by layer from the inside to the outside. The seepage field and stress field interact with each other, and the pore water pressure and stress are coupled with each other, resulting in increasingly complete fracture development.
- (3) The random distribution of quartz minerals in shale affects the distribution of mechanical parameters in shale specimens, causing asymmetry of crack extension. The rupture process reveals that the shale model mainly undergoes three stages: initial crack initiation, crack expansion and destabilization. The final damage mode is divided into “Y” and “X”.
- (4) The evolution of the acoustic emission signal distribution is characterized by three types. In the first category (0.2 MPa, 0.25 MPa, 0.3 MPa, 0.35 MPa, and 0.5 MPa), the cumulative AE shows the pattern of “flat–jump–flat–surge–flat”, in the second category (0.4 MPa), the cumulative AE shows the pattern of “flat–surge–stable”, and in the third category (0.45 MPa), the cumulative AE shows the pattern of “flat–jump–flat–surge–stable”. For the second category (0.4 MPa), the cumulative AE shows a “flat–jump–flat–surge–steady” pattern, and for the third category (0.45 MPa), the cumulative AE shows a “flat–jump–flat–surge–flat” pattern. In the third category

(0.45 MPa), the cumulative AE shows a pattern of “flat–jump growth”, and in the third category (0.45 MPa), the cumulative AE shows a pattern of “flat–jump growth”.

**Acknowledgements** This study was supported by the National Natural Science Foundation of China (Project No.52104080, No. 52264004); Guizhou Science and Technology Fund(Project No. [2021]401); Guizhou Science and Technology Fund (Qiankehe Support [2023] 136); Guizhou Science and Technology Fund (Qiankehe Support [2022] 227); Guizhou Science and Technology Fund (Qiankehe strategic search for minerals [2022] ZD005); Guizhou Province Outstanding Young Scientific and Technological Talents Training Plan (Project NO. Qian Kehe Platform Talents-YQK[2023]012); Natural Science Special (Special Post) Scientific Research Fund Project of Guizhou University (Project No. Guizhou University Special Post (2021) 51); Scientific Research Project of Guiyang Rail Transit Line 2 Phase I Project (Project No. D2(I)—FW—YJ—2019—001—WT), Guizhou Province, China [2021] 4023.Guizhou Mining Power Disaster Early Warning and Control Technology Innovation Team, China (Project No. 2019-5619).

**Author contributions** XX: Software, data curation, methodology, writing-original draft. ZW: Conceptualization, project administration, supervision. HS: Supervision, writing-review and editing. WW: Supervision, writing-review and editing. HC: Investigation. MT: Investigation. All authors reviewed the manuscript.

**Funding** This study was supported by the National Natural Science Foundation of China (Project No.52104080, No. 52264004); Guizhou Science and Technology Fund(Project No. [2021]401); Guizhou Science and Technology Fund (Qiankehe Support [2023] 136); Guizhou Science and Technology Fund (Qiankehe Support [2022] 227); Guizhou Science and Technology Fund (Qiankehe strategic search for minerals [2022] ZD005); Guizhou Province Outstanding Young Scientific and Technological Talents Training Plan (Project NO. Qian Kehe Platform Talents-YQK[2023]012); Natural Science Special (Special Post) Scientific Research Fund Project of Guizhou University (Project No. Guizhou University Special Post (2021) 51); Scientific Research Project of Guiyang Rail Transit Line 2 Phase I Project (Project No. D2 (I)—FW—YJ—2019—001—WT), Guizhou Province, China [2021] 4023.Guizhou Mining Power Disaster Early Warning and Control Technology Innovation Team, China (Project No. 2019-5619).

**Data availability** Some or all data, models, or codes generated or used during the study are available from the corresponding author by request.

### Declarations

**Conflict of interest** The authors have the appropriate permission from responsible authorities to do the study on-site and have no conflict of interest.

**Ethical approval** Not applicable.

**Consent for publication** All authors of this article consent to publish.

**Open Access** This article is licensed under a Creative Commons Attribution 4.0 International License, which permits use, sharing, adaptation, distribution and reproduction in any medium or format, as long as you give appropriate credit to the original author(s) and the source, provide a link to the Creative Commons licence, and indicate if changes were made. The images or other third party material in this article are included in the article's Creative Commons licence, unless indicated otherwise in a credit line to the material. If material is not included in the article's Creative Commons licence and your intended use is not permitted by statutory regulation or exceeds the permitted use, you will need to obtain permission directly from the copyright holder. To view a copy of this licence, visit <http://creativecommons.org/licenses/by/4.0/>.

## References

- Alafnan S (2022) Utilization of supercritical carbon dioxide for mechanical degradation of organic matters contained in shales. *Fuel J Fuel Sci* 316:123427
- Arthur JL, Asiedu-Okantah SA (2021) A review of the causes of sustainable supply deficiencies in natural gas supply in Ghana. *Electr Energy* 9:20
- Bu L, Li S, Shi S et al (2019) Numerical investigation to influence of perforation angle on hydraulic fracturing process. *Geotech Geol Eng* 37:1125–1133
- Chai D, Yang G, Fan Z et al (2019) Gas transport in shale matrix coupling multilayer adsorption and pore confinement effect. *Chem Eng J* 370:1534
- Changtao Y, Shuyuan L, Linyue L et al (2017) Study on desorption properties of shale gas. *Geoscience* 31:150
- Duan JC, Tang CA, Chang X et al (2006) Study on mechanics behavior of containing holes in brittle material subjected to uniaxial compression. *Rock Soil Mech* 27:1416–1420
- Gu Y, Ding W, Yin M et al (2019) Nanoscale pore characteristics and fractal characteristics of organic-rich shale: an example from the lower Cambrian Niutitang formation in the Fenggang block in northern Guizhou Province, South China. *Energy Explor Exploit* 37(1):273
- He X, Wu J, Yong R, Zhao S (2021) Hydrocarbon accumulation and key exploration & development technologies of Changning-Weiyuan marine shale gas field, southern Sichuan. *Pet Res* 6:1
- Iqbal O, Padmanabhan E, Mandal A et al (2021) Characterization of geochemical properties and factors controlling the pore structure development of shale gas reservoirs. *J Pet Sci Eng* 206:109001
- Jiang JWH (2016) Experimental and numerical study on hydraulic fracture propagation in coalbed methane reservoir. *J Nat Gas Sci Eng* 35:455
- Jiu K, Ding WL, Huang WH et al (2013) Fractures of lacustrine shale reservoirs, the Zhanhua Depression in the Bohai Bay Basin, eastern China. *Mar Pet Geol* 48:113–123
- Kazemi M, Takhiri-Borujeni A, Hansel JR (2019) Enhanced oil recovery of shale oil: a molecular simulation study. In: *Unconventional resources technology conference*
- Ke-Wei F, Han C, Jie-Neng S et al (2015) Research on the influence of PH on the performance of SDBS fracturing fluid suitable for shale gas reservoir. *Explor Eng*
- Li D, Wang Y, Zeng B et al (2021) Optimization of the shale gas reservoir fracture parameters based on the fully coupled gas flow and effective stress model. *Energy Sci Eng* 9:676
- Liu X, Zhuang Y, Liang L et al (2019) Investigation on the influence of water-shale interaction on stress sensitivity of organic-rich shale. *Geofluids* 2019:1–13
- Liu H, Zheng LL, Zuo YJ et al (2021a) Study on mesoscopic damage evolution characteristics of single joint sandstone based on micro-CT image and fractal theory. *Shock Vib* 2021:1–18
- Liu H, Zuo YJ, Wu ZH et al (2021b) Fractal analysis of mesoscale failure evolution and microstructure characterization for sandstone using DIP, SEM-EDS, and micro-CT. *Int J Geomech* 21(9):04021153
- Liu H, Wu ZH, Zuo YJ et al (2023a) Fractal study on meso-damage evolution of three-dimensional irregular fissured sandstone. *Int J Geomech* 23(11):04023199
- Liu H, Mukherjee B, Zuo Y et al (2023b) Fractal dimension used as a proxy to understand the spatial distribution for carlin-type gold deposits. *Ore Geol Rev* 158:105534
- Liu H, Zuo YJ, Rodriguez-Dono A et al (2023c) Study on multi-period palaeotectonic stress fields simulation and fractures distribution prediction in Lannigou gold mine, Guizhou. *Geomech Geophys Geo-Energy Geo-Resour* 9(1):92
- Ma S, Guo J, Li L et al (2016) Experimental and numerical study on fracture propagation near open-hole horizontal well under hydraulic pressure. *Revue Francaise De Gnie Civ* 20:412–430
- Noghabai K (1999) Discrete versus smeared versus element-embedded crack models on ring problem. *J Eng Mech* 125:307–315
- Olson JE (2015) Predicting fracture swarms: the influence of subcritical crack growth and the crack-tip process on joint spacing in rock. *Geol Soc London Special Publ* 231:73–88
- Orozco D, Aguilera R, Selvan K (2018) Material balance forecast of huff-and-puff gas injection in multiporosity shale oil reservoirs. In: *SPE Canada unconventional resources conference*
- Pan Z, Connell LD (2015) Reservoir simulation of free and adsorbed gas production from shale. *J Nat Gas Sci Eng* 22:359–370
- Rabczuk T, Zi G, Bordas S et al (2010) A simple and robust three-dimensional cracking-particle method without enrichment. *Comput Methods Appl Mech Eng* 199:2437–2455
- Ross DJK, Bustin RM (2009) The importance of shale composition and pore structure upon gas storage potential of shale gas reservoirs. *Mar Pet Geol* 26:916–927
- Slatt RM, Rodriguez ND (2012) Comparative sequence stratigraphy and organic geochemistry of gas shales: commonality or coincidence? *J Nat Gas Sci Eng* 8:68



- Song HL, Wu ZH, Wang AL et al (2020) Study on the micro-scale tensile properties of lower cambrian niutitang formation shale based on digital images. *Geofluids*
- Tang C, Tham L, Lee P et al (2002) Coupled analysis of flow, stress and damage (FSD) in rock failure *International. J Rock Mech Min Sci* 39:477–489
- Tang CA, Wong RHC, Chau KT et al (2005) Modeling of compression-induced splitting failure in heterogeneous brittle porous solids. *Eng Fract Mech* 72:597–615
- Thallak S, Rothenburg L, Dusseault M (1991) Simulation of multiple hydraulic fractures in a discrete element system. *American Rock Mechanics Association*
- Tong X, Wen H, Cheng X et al (2021) Characteristics of pressure relief gas extraction in the protected layer by surface drilling in Huainan. *Adv Civ Eng* 2021:1–11
- Wang R, Ding W, Zhang Y et al (2016a) Analysis of developmental characteristics and dominant factors of fractures in Lower Cambrian marine shale reservoirs: a case study of Niutitang formation in Cen'gong block, southern China. *J Petrol Sci Eng* 138:31
- Wang Y, Li X, Zhou RQ et al (2016b) Numerical evaluation of the effect of fracture network connectivity in naturally fractured shale based on FSD model. *Sci China Earth Sci* 59:626
- Wang W, Wu Z, Song H et al (2022) Study on the failure mechanism of lower cambrian shale under different bedding dips with thermosolid coupling. *Geofluids* 2022:1–15
- Weng X, Kresse O, Cohen C et al (2011) Modeling of hydraulic-fracture-network propagation in a naturally fractured formation. *Spe Prod Oper* 26:368–380
- Wu ZH, Song HL, Li LP et al (2021) Study on the damage evolution process and fractal of quartz-filled shale under thermal-mechanical coupling. *Geofluids*
- Wu Z, Yang Y, Zuo Y et al (2023) Damage evolution characteristics of 3D reconstructed bedding-containing shale based on CT technology and digital image processing. *Acta Geophys*
- Xu T, Tang CA, Yang TH et al (2006) Numerical investigation of coal and gas outbursts in underground collieries. *Int J Rock Mech Min Sci* 43(6):905–919
- Xu T, Ranjith PG, Au AS, Wasantha PL, Yang TH, Tang CA, Liu HL, Chen CF (2015) Numerical and experimental investigation of hydraulic fracturing in Kaolin clay. *J Pet Sci Eng* 134:223
- Yakaboylu GA, Gupta N, Sabolsky EM et al (2020) Mineralogical characterization and strain analysis of the Marcellus shales. *Int J Rock Mech Min Sci* 130:104345
- Yaoru L, Feng'E Z, Jixiang Q et al (2002) Evaporite karst and resultant geohazards in China. *Carbon Evap* 17:159–165
- Yu W, Xiao LI, Runqing Z et al (2016) Numerical evaluation of the shear stimulation effect in naturally fractured formations. *Sci China Earth Sci* 000:371–383
- Yu X, Liu H, Cui S et al (2021) Study on the mechanism and main control factors of lost circulation in deep brittle shale in Changning block. *IOP Conf Ser Earth Environ Sci* 861:62078
- Zhang R et al (2019) Experimental investigation on fracture morphology in laminated shale formation by hydraulic fracturing. *J Pet Sci Eng* 177:442
- Zhang J, Li X, Zou X et al (2020) Characterization of multi-type pore structure and fractal characteristics of the Dalong Formation marine shale in northern Sichuan Basin. *Energy Sources* 42:2764
- Zhao Q, Lisjak A, Mahabadi O et al (2014) Numerical simulation of hydraulic fracturing and associated microseismicity using finite-discrete element method. *J Rock Mech Geotech Eng* 6:574
- Zhigang Y, Hongtu W, Nianping L et al (2012) Simulation study of characteristics of hydraulic fracturing propagation of low permeability coal seam. *Disast Adv* 5:717–720
- Zou C, Dong D, Wang Y et al (2016) Shale gas in China: characteristics, challenges and prospects (II). *Pet Explor Dev* 43:182–196

**Publisher's Note** Springer Nature remains neutral with regard to jurisdictional claims in published maps and institutional affiliations.